Letter Vol. 7, No. 10 / October 2020 / Optica 1275

optica

# Near-octave lithium niobate soliton microcomb

Zheng Gong, Xianwen Liu, Yuntao Xu, and Hong X. Tang*

*Department of Electrical Engineering, Yale University, New Haven, Connecticut 06511, USA*
**Corresponding author: hong.tang@yale.edu*

*Received 24 June 2020; revised 8 August 2020; accepted 11 August 2020 (Doc. ID 400994); published 28 September 2020*

**Thin film lithium niobate (LN) is bringing renewed potential to the realm of integrated photonics. Its strong quadratic and cubic nonlinearities as well as wide transparency window are ideal for realizing on-chip self-referenced soliton microcombs. However, broadband Kerr cavity soliton generation in LN thin films remains challenging due to limited dispersion control and competition from strong stimulated Raman scattering (SRS). Here, we demonstrate the generation of soliton microcombs in LN thin films featuring broad spectral spans up to 4/5 octaves with the emission of dual dispersion waves (2/3 octaves apart) and sub-terahertz repetition rates (down to 335 GHz) by suppressing strong SRS. Numerical simulations based on coupled-mode equations that incorporate Raman effects further elucidate the soliton dynamics in this highly Raman-active material system.** 

https://doi.org/10.1364/OPTICA.400994

Broadband chip-based Kerr cavity solitons offer highly coherent microcomb sources and have enabled a wide range of applications [1,2]. Under micro-scale optical confinement and sharp refractive index contrast, the soliton microcomb bandwidth can be widely tuned through dispersion engineering [3]. Cherenkov radiations resulting from higher-order dispersion [4] can be further utilized to expand the soliton bandwidth [5,6]. While the dispersion control is effective in promoting soliton generation and increasing its bandwidth, the competition between the soliton and other nonlinear effects, such as stimulated Raman scattering (SRS) [7–15], could become a limiting factor for broadband soliton comb generation.

Among many comb materials, lithium niobate (LN)-on-insulator has gained particular interest [9,14,16], owing to its strong $\chi^{(2)}$ and $\chi^{(3)}$ nonlinearities as well as its broad transparency window. Photonic components such as highly efficient frequency doublers [17–19] and broadband electro-optic modulators [20] have been integrated on this platform. Electrically assisted domain-poling [17–19] provides an additional degree of freedom for controlling the nonlinear coupling between fundamental and harmonic modes. All of these advantages distinguish LN thin films as a highly desirable platform to realize on-chip soliton microcomb self-referencing via either the $2f-3f$ [21] or $f-2f$ [22] scheme.

In this Letter, we demonstrate broadband soliton microcombs in microrings patterned on $z$-cut LN-on-insulator thin films (NanoLN). We show that by tailoring the microring geometry, especially its height, favorable dispersion can be realized for the emission of dual dispersion waves (DWs) to expand the soliton bandwidth to 4/5 octaves. Such broad bandwidth soliton makes on-chip $2f-3f$ self-referencing feasible. LN is highly Raman-active, possessing multiple (up to 26) Raman modes [23], which leads to low threshold SRS disrupting the soliton formation [9,16]. For effective mitigation of SRS, we establish an analytical model to estimate the intracavity SRS threshold and identify suitable microring-waveguide coupling strength [24] to raise the SRS threshold and promote soliton generation. Numerical simulations based on coupled-mode equations that incorporate the Raman effect are carried out to elucidate the underlying intracavity dynamics.

Broadband microcomb generation [3] critically relies on the engineering of the microresonator dispersion profile, which can be quantified by the integrated dispersion curve [25] $D_{\mathrm{int},\mu}=\sum_n \mu^n/(n!)\,D_n$, with $D_n$ denoting the $n^{\mathrm{th}}$-order dispersion coefficient. By optimizing the microring geometry, higher-order dispersion has been successfully exploited in $Si_3N_4$ microrings to obtain dual DWs for efficient extension of the soliton bandwidth [5,6]. We adopt the partially etched air-clad waveguide structure and use numerical simulations to identify microring geometries that favor broadband soliton generation. As illustrated by the schematic in Fig. 1(a), a trapezoid delineates the upper cross-sectional profile of the LN waveguide to factor in the sidewall angle resulting from the plasma dry etch process [16] [estimated as 30° from the scanning electron microscope (SEM) image in Fig. 1(b)]. Sitting beneath the trapezoid is a slab of ~200-nm-thick LN. The microring radius is also considered in the dispersion simulations.

The main degrees of freedom used to obtain favorable dispersion profiles are the microring top width ($W$), the total thickness of the LN layer ($H$), and the microring radius ($R$). A series of simulated $D_{\mathrm{int}}$ curves are presented in Figs. 1(c) and 1(d) with a fixed radius of $R=60$ μm as examples to illustrate the optimization process. As indicated by Fig. 1(c), the waveguide height $H$ significantly impacts the dispersion at lower frequencies, which can lead to large frequency shift of the red-side DW (near the left zero-crossing point of the $D_{\mathrm{int}}$ curve [26]). The blue-side DW, on the other hand, is pushed outward in a relatively steady manner as $H$ is increased. Although widely separated DWs can be achieved from taller microrings, the huge hump of the $D_{\mathrm{int}}$ curve could render the intermediate comb lines weak, as evidenced by the simulated soliton output spectra shown in Fig. 1(e), where the DWs intensities also drop considerably [27]. The simulated $D_{\mathrm{int}}$ curves with varying $H$ suggest that when $H$ is set near 0.56 μm,

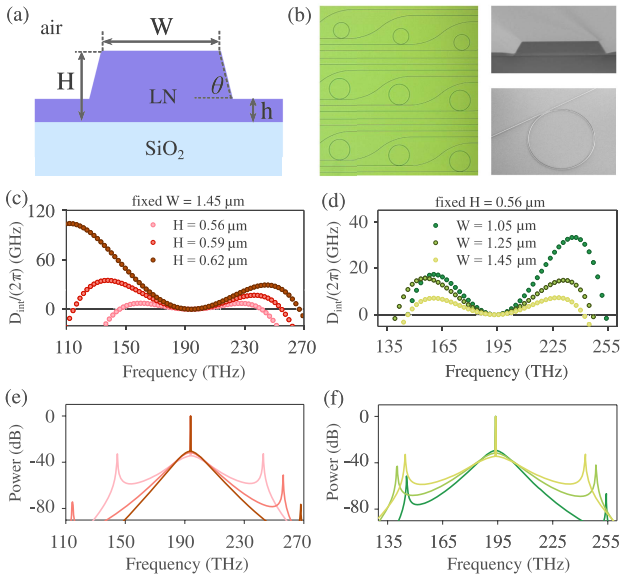


**Fig. 1.** (a). Cross-sectional schematic of the $z$-cut LN waveguide. $H$, LN layer thickness; $W$, microring top width; $\theta$, sidewall angle; $h$, LN slab thickness. (b) Optical and SEM images of partially etched, air-cladded devices. (c) and (d) Simulated $D_{\text{int}}$ curves as a function of frequency for (c) different $H$'s) and (d) different $W$'s. (e) and (f) Simulated soliton output spectra corresponding to the $D_{\text{int}}$ curves in (c) and (d), respectively. All modes are set to have the same intrinsic decay rates $\kappa_i/(2\pi) = 190$ MHz and external coupling rates $\kappa_e = \kappa_i$. An on-chip pump power of 240 mW was used. The Raman effect was neglected in the simulation.

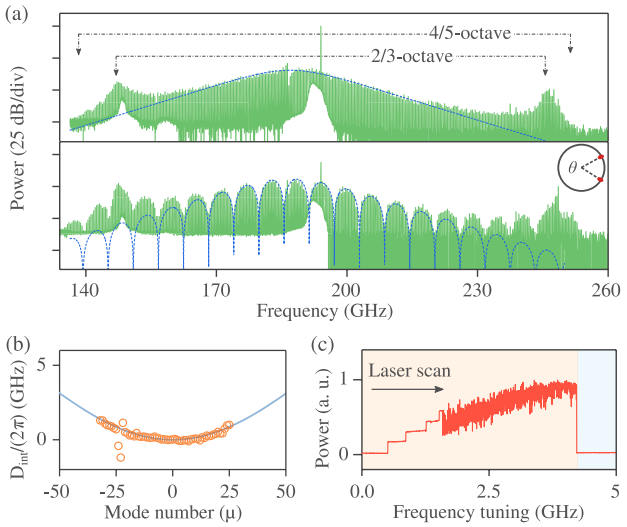


**Fig. 2.** (a) Normalized output spectra of the single-soliton and the two-soliton microcombs. Dashed line in the upper (lower) panel: a sech$^2$ fitting curve (with sinusoidal modulation). Inset: relative positions of the solitons inside the cavity ($\theta \approx 21°$). On-chip pump powers of 240 mW and 270 mW were used, respectively. (b) The extracted $D_{\text{int}}$ curve (yellow circles) with the simulated one (blue line) around the pump versus mode number $\mu$. (c) Comb power trace versus pump frequency tuning. The pump was scanned from the red side (shaded red region) to the blue side (shaded blue region) of the resonance at a speed of 62.5 GHz/s.

the trade-off between the DW spacing and accessible comb line power can be well balanced, leading to the emission of comparably strong dual DWs 2/3 octaves apart. During fabrication, $H$ was tailored by an optimized plasma thin-down process [16]. After selecting a suitable thickness $H$, one can then adjust $W$ to tune the DWs frequencies [Figs. 1(d) and 1(f)].

In addition to dispersion engineering, it is also necessary to consider strong Raman effects in LN, where multiple (26) Raman-active vibrational modes with different frequencies (4 to 26 THz) and linewidths ($10^2$ to $10^3$GHz) are present [23]. The strong Raman gain (up to 1.3 cm/GW at 1.55 μm [9]) leads to low threshold SRS, which prohibits soliton generation [9,16]. To favor the formation of a soliton over SRS in a microring, we need to raise the intracavity pump mode threshold energy for SRS ($\varepsilon_{\text{th,R}}$) above the threshold energy for a soliton ($\varepsilon_{\text{th,S}}$). This is achieved by adjusting the external coupling rate ($\kappa_e$) relative to the intrinsic decay rate ($\kappa_i$). The values of $\varepsilon_{\text{th,R}}$ and $\varepsilon_{\text{th,S}}$ are estimated by the analytical models described in Supplement 1.

For example, we attempt to generate a soliton microcomb with a FWHM of 14 THz (2/3 octave bandwidth at 38 dB below the peak of its envelope) from a straight-waveguide coupled microring ($H = 0.56$ μm, $W = 1.45$ μm, $R = 60$ μm). Assuming a constant $\kappa_i$ [$(2\pi)$190 MHz] and $\kappa_e$ over the modes of interest, $\kappa_e$ should be made smaller than $2.2\kappa_i$ in order to have $\varepsilon_{\text{R,th}} > \varepsilon_{\text{S,th}}$ (see Supplement 1 for a detailed calculation). In the experiment, $\kappa_e$ was adjusted by varying the coupling gap so that the microring exhibited $\kappa_e \approx 1.3\kappa_i$, which favored soliton generation over SRS [Fig. (2)]. In contrast, only SRS was generated in the microring of the same geometry without the control of $\kappa_e$ (see Supplement 1).

The strong photorefractive effect in LN allows direct soliton mode-locking with simple red-detuned laser scans as demonstrated previously in $z$-cut LN microrings [14,16]. A broadband single-soliton microcomb was obtained from a microring with $H = 0.56$ μm, $W = 1.45$ μm, and $R = 60$ μm. The upper panel in Fig. 2(a) shows its output spectrum possessing a sub-terahertz (THz) repetition rate of 335 GHz and a total span of 112 THz. This span corresponds to 4/5 of an octave above the noise floor of the optical spectrum analyzer. A FWHM of 14 THz is extracted by fitting the spectral envelope with a sech$^2$ function. The generated DWs, separated by the 2/3 octave, enhance the comb line power near both edges of the spectrum and thus contribute to the extension of the soliton bandwidth. The DW frequencies are consistent with the predictions based on the simulated $D_{\text{int}}$ curve of the microring [Fig. 1(d)]. The dispersion profile of the microring was measured [28] and shown in Fig. 2(b), which reveals $D_2 \approx 2.6$ MHz. The abrupt change of the measured $D_{\text{int}}$ curve around the mode of $\mu = -23$ could be caused by a local avoided mode crossing [29].

Moreover, multiple soliton states were excited, as indicated by the step pattern in a measured comb power trace [Fig. 2(c)]. The bottom panel in Fig. 2(a) presents an output spectrum of a two-soliton microcomb, which features a typical sinusoidal modulation over its envelope [25]. By fitting the modulated spectral profile, a time interval of 0.17 ps between the pulses is inferred. Additionally, the blue-side DW shifted toward higher frequencies in comparison with the single-soliton case. An increase in the pump-to-comb conversion efficiency was also observed [6].

For applications that demand strong comb line power at targeted frequencies, e.g., building an on-chip interface with an atomic system utilizing DWs [30], it is often desirable that the platform allows fine adjustments of the DW frequencies. We demonstrate that the spectral positions of DWs can be widely

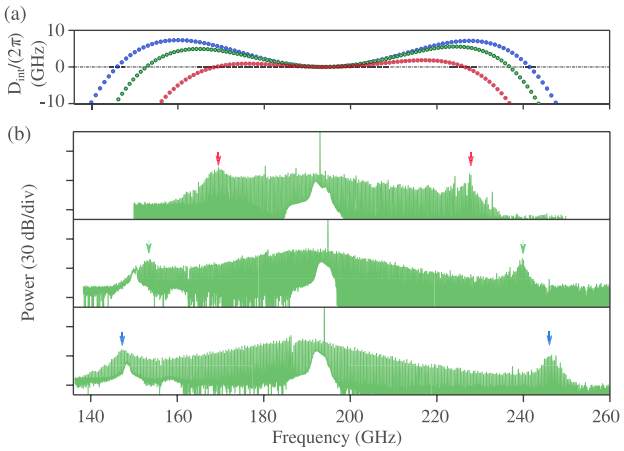


**Fig. 3.** (a) Simulated $D_{int}$ curves for microrings of $H = 0.55$ μm, $W = 1.45$ μm, $R = 65$ μm (red); $H = 0.56$ μm, $W = 1.55$ μm, $R = 70$ μm (green); and $H = 0.56$ μm, $W = 1.45$ μm, $R = 60$ μm (blue). (b) Normalized soliton output spectra obtained from microrings of the geometries listed in (a). The peaks of the DWs are marked by arrows of the same colors as the corresponding $D_{int}$ curves. On-chip pump powers of 165 mW, 200 mW, and 240 mW were used, respectively.

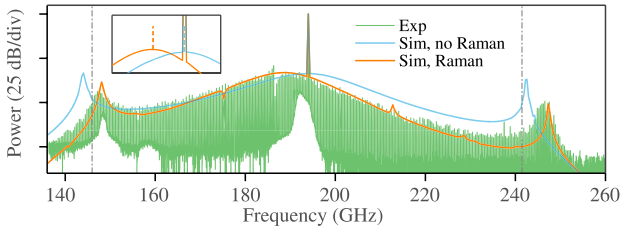


**Fig. 4.** Simulated soliton output spectral profile without/with Raman effect (blue/orange) in comparison with the measured spectrum [green, same as Fig. 2(a)]. Dash-dotted lines indicate the zero-crossing points of the corresponding simulated $D_{int}$ curve. An on-chip pump power of 240 mW was used for all. Inset: zoom-in view of the simulated spectra with dashed lines marking the spectral centers.

varied on this LN thin-film platform through dispersion engineering. As shown by the simulations in Fig. 3(a), one can flexibly alter the profile of the $D_{int}$ curve to yield different zero-crossing points, i.e., approximate spectral positions for DW emission [26], by varying the microring geometry.

Microcomb spectra with different DW emission frequencies are shown in Fig. 3(b), obtained from microrings of the targeted geometries. The spectral positions of those DWs trend well with the predictions in Fig. 3(a). In total, a ∼20 THz shift in the DW frequency was achieved on both sides, while the comb bandwidth increased significantly through the extension of DWs. Notable blue shifts of the blue-side DWs relative to the zero-crossing points of the $D_{int}$ curves were also observed and could be attributed to Kerr self-phase modulation [26,30] as well as the Raman effect [29]. Similar phenomena were also observed in our numerical simulations presented in Fig. 4. To finely adjust DW frequency, one can either vary the microring geometry using small increments or electro-optically tune the effective index. The electro-optical tuning can be implemented by applying electric fields along the $z$ axis ($\gamma_{33} = 30$ pm/V [20]) via suspended electrodes over the waveguide without impacting its dispersion or by applying in-plane electric fields along the $y$ axis [31], which is less efficient than tuning $x$-cut devices [20], but still benefits from a relatively large $\gamma_{22} = 5.6$ pm/V of LN [31].

To simulate the dynamics of Kerr cavity solitons in highly Raman-active LN microrings, we incorporate the Raman effect into the coupled-mode equations [25] (see Supplement 1). The simulation results presented in Fig. 4 reveal the impacts of the Raman effect on the soliton spectrum. For the sake of comparison, we first neglected the Raman effect to simulate the soliton output spectrum. The spectral center of the soliton turned out to be close to the pump frequency, while the DWs experienced a red shift of ∼1.9 THz and a blue shift of ∼0.9 THz, respectively, relative to the predicted positions (dashed vertical lines) under a linear approximation ($D_{int,\mu} = 0$) [26]. This can be understood by considering that the radiations from the DWs induce soliton recoils of opposite directions that counteract each other [27]. Consequently, the soliton spectral center remained around the pump frequency.

With the presence of the Raman effect in the simulation, intrapulse Raman scattering caused additional energy transfer from higher to lower frequency components of the soliton [12–14], which shifted the soliton spectral center toward the red side by ∼5.3 THz. This frequency shift also introduced a decrease in the soliton group velocity [13,27] and thus altered the DW phase-matching condition [13]. As a result, both DWs were blue shifted. In the end, the blue-side DW experienced larger net blue shift than the red-side DW, agreeing well with the measured spectrum.

In conclusion, we demonstrate broadband (up to 4/5 octaves) soliton microcombs with sub-THz repetition rates (down to 335 GHz) from LN microrings by leveraging the higher-order dispersion induced dual DW emissions. We show that the spacing between the dual DWs is widely variable through tailoring the microring geometry on this platform. We also analytically estimate the SRS threshold and identify suitable external coupling strength to promote soliton generation.

We believe such broadband soliton microcombs with engineered dual DW emissions and a relatively low free spectral range (FSR) mark an important step toward on-chip soliton microcomb self-referencing on a LN thin film platform. Meanwhile, we recognize challenges in further broadening the microcomb bandwidth, such as the rapidly increasing $D_{int}$ in thicker LN films around the red-side DW and the drop in intrinsic $Q_{in}$ caused by the thin-down process. We anticipate that octave spanning soliton microcombs are attainable with increased $Q_{in}$ (see Supplement 1) and appropriate external coupling strength to suppress SRS. Additionally, there is also the possibility to extend our broadband soliton microcombs into the visible band via intracavity $\chi^{(2)}$-doubling and $\chi^{(3)}$-tripling effects, as shown in [32,33].

**Funding.** David and Lucile Packard Foundation; Sandia National Laboratories (DENA0003525 under proposal 052181 213-1); Defense Advanced Research Projects Agency (HR0011-16-C-0118).

**Acknowledgment.** The authors thank Dr. Ming Li and Dr. Chang-ling Zou for efforts in building the initial numerical models used in this work, and Dr. Michael Rooks, Michael Power, Yong Sun, Sean Rinehart, and Kelly Woods for assistance in device fabrication at the Yale cleanroom.

**Disclosures.** The authors declare no conflicts of interest.

See Supplement 1 for supporting content.

## REFERENCES


1. A. L. Gaeta, M. Lipson, and T. J. Kippenberg, Nat. Photonics **13**, 158 (2019).
2. T. J. Kippenberg, A. L. Gaeta, M. Lipson, and M. L. Gorodetsky, Science **361**, eaan8083 (2018).
3. Y. Okawachi, M. R. E. Lamont, K. Luke, D. O. Carvalho, M. Yu, M. Lipson, and A. L. Gaeta, Opt. Lett. **39**, 3535 (2014).
4. V. Brasch, M. Geiselmann, T. Herr, G. Lihachev, M. H. P. Pfeiffer, M. L. Gorodetsky, and T. J. Kippenberg, Science **351**, 357 (2016).
5. Q. Li, T. C. Briles, D. A. Westly, T. E. Drake, J. R. Stone, B. R. Ilic, S. A. Diddams, S. B. Papp, and K. Srinivasan, Optica **4**, 193 (2017).
6. M. H. P. Pfeiffer, C. Herkommer, J. Liu, H. Guo, M. Karpov, E. Lucas, M. Zervas, and T. J. Kippenberg, Optica **4**, 684 (2017).
7. Y. Okawachi, M. Yu, V. Venkataraman, P. M. Latawiec, A. G. Griffith, M. Lipson, M. Lončar, and A. L. Gaeta, Opt. Lett. **42**, 2786 (2017).
8. H. Jung, Z. Gong, X. Liu, X. Guo, C. L. Zou, and H. X. Tang, Opt. Express **27**, 22246 (2019).
9. M. Yu, Y. Okawachi, R. Cheng, C. Wang, M. Zhang, A. L. Gaeta, and M. Lončar, Light Sci. Appl. **9**, 9 (2020).
10. P. Latawiec, V. Venkataraman, M. J. Burek, B. J. M. Hausmann, I. Bulu, and M. Lončar, Optica **2**, 924 (2015).
11. D. J. Wilson, K. Schneider, S. Hoenl, M. Anderson, T. J. Kippenberg, and P. Seidler, Nat. Photonics **14**, 57 (2020).
12. M. Karpov, H. Guo, A. Kordts, V. Brasch, M. H. P. Pfeiffer, M. Zervas, M. Geiselmann, and T. J. Kippenberg, Phys. Rev. Lett. **116**, 103902 (2016).
13. X. Yi, Q.-F. Yang, K. Y. Yang, M.-G. Suh, and K. J. Vahala, Optica **2**, 1078 (2015).
14. Y. He, Q.-F. Yang, J. Ling, R. Luo, H. Liang, M. Li, B. Shen, H. Wang, K. J. Vahala, and Q. Lin, Optica **6**, 1138 (2019).
15. Z. Gong, A. Bruch, M. Shen, X. Guo, H. Jung, L. Fan, X. Liu, L. Zhang, J. Wang, J. Li, J. Yan, and H. X. Tang, Opt. Lett. **43**, 4366 (2018).
16. Z. Gong, X. Liu, Y. Xu, M. Xu, J. B. Surya, J. Lu, A. Bruch, C. Zou, and H. X. Tang, Opt. Lett. **44**, 3182 (2019).
17. R. Luo, Y. He, H. Liang, M. Li, and Q. Lin, Optica **5**, 1006 (2018).
18. C. Wang, C. Langrock, A. Marandi, M. Jankowski, M. Zhang, B. Desiatov, M. M. Fejer, and M. Lončar, Optica **5**, 1438 (2018).
19. J. Lu, J. B. Surya, X. Liu, A. W. Bruch, Z. Gong, Y. Xu, and H. X. Tang, Optica **6**, 1455 (2019).
20. M. Zhang, B. Buscaino, C. Wang, A. Shams-Ansari, C. Reimer, R. Zhu, J. M. Kahn, and M. Lončar, Nature **568**, 373 (2019).
21. V. Brasch, E. Lucas, J. D. Jost, M. Geiselmann, and T. J. Kippenberg, Light Sci. Appl. **6**, e16202 (2017).
22. P. Del'Haye, A. Coillet, T. Fortier, K. Beha, D. C. Cole, K. Y. Yang, H. Lee, K. J. Vahala, S. B. Papp, and S. A. Diddams, Nat. Photonics **10**, 516 (2016).
23. A. S. Barker and R. Loudon, Phys. Rev. **158**, 433 (1967).
24. Y. Zheng, C. Sun, B. Xiong, L. Wang, J. Wang, Y. Han, Z. Hao, H. Li, and Y. Luo, *Conference on Lasers and Electro-Optics* (Optical Society of America, 2019), paper JTu2A.90.
25. T. Herr, V. Brasch, J. D. Jost, C. Y. Wang, N. M. Kondratiev, M. L. Gorodetsky, and T. J. Kippenberg, Nat. Photonics **8**, 145 (2014).
26. D. Skryabin and Y. Kartashov, Opt. Express **25**, 27442 (2017).
27. A. V. Cherenkov, V. E. Lobanov, and M. L. Gorodetsky, Phys. Rev. A **95**, 033810 (2017).
28. S.-W. Huang, H. Zhou, J. Yang, J. F. McMillan, A. Matsko, M. Yu, D.-L. Kwong, L. Maleki, and C. W. Wong, Phys. Rev. Lett. **114**, 053901 (2015).
29. Q.-F. Yang, X. Yi, K. Y. Yang, and K. J. Vahala, Optica **3**, 1132 (2016).
30. S.-P. Yu, T. C. Briles, G. T. Moille, X. Lu, S. A. Diddams, K. Srinivasan, and S. B. Papp, Phys. Rev. Appl. **11**, 044017 (2019).
31. A. Yariv, P. Yariv, and P. Yeh, *Photonics: Optical Electronics in Modern Communications*, Oxford series in electrical and computer engineering (Oxford University, 2007).
32. H.-J. Chen, Q.-X. Ji, H. Wang, Q.-F. Yang, Q. Cao, Q.-T. Gong, X. Yi, and Y.-F. Xiao, Nat. Commun. **11**, 2336 (2020).
33. H. Jung, R. Stoll, X. Guo, D. Fischer, and H. X. Tang, Optica **1**, 396 (2014).